APPLIED SCIENCES AND ENGINEERING

Magnetosensitive e-skins with directional perception for augmented reality

Gilbert Santiago Cañón Bermúdez,[1,2]* Dmitriy D. Karnaushenko,[2] Daniil Karnaushenko,[2] Ana Lebanov,[1] Lothar Bischoff,[1] Martin Kaltenbrunner,[3] Jürgen Fassbender,[1] Oliver G. Schmidt,[2,4] Denys Makarov[1,2]*

Electronic skins equipped with artificial receptors are able to extend our perception beyond the modalities that have naturally evolved. These synthetic receptors offer complimentary information on our surroundings and endow us with novel means of manipulating physical or even virtual objects. We realize highly compliant magnetosensitive skins with directional perception that enable magnetic cognition, body position tracking, and touchless object manipulation. Transfer printing of eight high-performance spin valve sensors arranged into two Wheatstone bridges onto 1.7-μm-thick polyimide foils ensures mechanical imperceptibility. This resembles a new class of interactive devices extracting information from the surroundings through magnetic tags. We demonstrate this concept in augmented reality systems with virtual knob-turning functions and the operation of virtual dialing pads, based on the interaction with magnetic fields. This technology will enable a cornucopia of applications from navigation, motion tracking in robotics, regenerative medicine, and sports and gaming to interaction in supplemented reality.

INTRODUCTION

State-of-the-art virtual or augmented reality systems rely on optical detection of moving body parts to enable the manipulation of virtual objects. This is typically achieved using camera arrays (for example, integrated in wearables), accelerometers, and compasses in conjunction with on-the-fly image processing. However, the resolution of these approaches is insufficient to reconstruct fine motions such as those associated with fingers being moved with respect to the palm because the onboard energy supply of wearable gadgets is typically too limited. Methods that use arrays of ultrasonic generators are equally energy-inefficient for wearables. Advancing beyond the bulky, heavy, and often restraining virtual reality sets of goggles and gloves that enable interaction with the virtual world calls for the realization of novel, skin-like human-machine interfaces (*1*–*3*).

We envision that lightweight, high conformability, and even mechanical imperceptibility (*4*–*7*) are the key characteristics for wearable (*8*–*14*) and on-skin (*15*–*19*) electronics of the prospective personal appliances that will form the interface between our physical world and supplemented reality. Imperceptible electronic skins (e-skins) capable of touchless interaction not only open exciting possibilities for business or the gaming industry but also are beneficial for safety and security applications. Here, the somatic manipulation of objects, for example, turning regulation knobs located in a restricted environment, is undesirable or even prohibited.

Realizing touchless manipulation of virtual objects requires at least two basic functions combined in a single gadget, namely, proximity sensing imitating the "touching" function and the detection of a spatial direction as a counterpart of the "turning" function. The first feature is achieved with magnetic field sensors that are in essence proximity sensors. We introduced this concept for wearable and on-skin electronics (*7*, *20*, *21*). However, these early demonstrations are unable to resolve directions in space.

Here, we introduce the first mechanically imperceptible e-skin equipped with magnetic functionality that is capable of tracking motions of the body. Unlike conventional optics-based concepts, our approach does not require a direct line of sight between a (virtual) object and the sensors. Based on the interaction with magnetic fields, our platform provides complementary information channels yet underexplored. Our devices operate at low power in conjunction with permanent magnets that do not require energy for operation. Applications range from navigation, motion tracking in robotics, regenerative medicine, and sports and gaming to interaction in supplemented reality (Fig. 1A). The e-skin monitors the motion of the body, for example, hand, when it is rotated with respect to the direction of the external magnetic field (Fig. 1, B and C). The angular position of the hand is digitized and can be readily displayed or even used to interact in a touchless way with objects in virtual or augmented reality. We demonstrate the concept in augmented reality systems with virtual knob-turning functions as well as the operation of virtual dialing pads. Realizing directional perception in ultrathin form factors requires fabricating a two-dimensional (2D) magnetic field sensor on a customized, temperature-stable 1.7-μm-thick polyimide-based foil allows for discriminating between the x and y in-plane components of the magnetic field. The 2D sensitivity is gained by designing a sensor consisting of two Wheatstone bridges accommodating in total eight sensing elements, each having a well-defined magnetic anisotropy axis. This is characteristic of spin valves (*22*)—magnetic switches operating based on the giant magnetoresistive (GMR) effect. The fabrication platform synergistically combines thin film and transfer printing technologies.

RESULTS AND DISCUSSION

2D magnetic field sensorics on ultrathin foils: Two Wheatstone bridges of spin valves

A spin valve sensor comprises a [Py/CoFe]/Cu/[CoFe/Py]/IrMn heterostructure, with IrMn acting as an antiferromagnet pinning the magnetization of the reference [CoFe/Py] bilayer adjacent to it due

[1]Helmholtz-Zentrum Dresden-Rossendorf e.V., Institute of Ion Beam Physics and Materials Research, Bautzner Landstrasse 400, 01328 Dresden, Germany. [2]Institute for Integrative Nanosciences, Leibniz Institute for Solid State and Materials Research Dresden (IFW Dresden), Helmholtzstrasse 20, 01069 Dresden, Germany. [3]Soft Electronics Laboratory, Linz Institute of Technology, Johannes Kepler University Linz, Altenbergerstrasse 69, 4040 Linz, Austria. [4]Material Systems for Nanoelectronics, Technische Universität Chemnitz, Reichenhainer Strasse 70, 09111 Chemnitz, Germany.
*Corresponding author. Email: g.canon-bermudez@hzdr.de (G.S.C.B.); d.makarov@hzdr.de (D.M.)

to exchange bias (EB) (*23*). The free layer [Py/CoFe] separated by a Cu spacer acts as the sensor layer. These structures are integrated in Wheatstone bridges with orthogonal sensitivity axes to realize entirely flexible 2D magnetic field sensors. Key processing steps are shown in Fig. 2A (the full fabrication flow is shown in fig. S1): The magnetic layer stack is deposited onto lithographically defined areas on a polymeric foil. We developed temperature-stable polyimide-based foils to comply with the need of temperature treatment of the sensor while processing. Only 1.7 μm thick, these foils assure mechanical imperceptibility and the highest possible conformability of the devices as needed for on-skin appliances. Despite their thinness, the foils can withstand long-term annealing at 300°C even when exposed to a constant stress and allow soldering to contact pads that are lithographically defined on a foil (Table 1). The foil is laminated onto a glass slide coated with a sacrificial layer for processing. We prepare an extended array of spin valves in a single deposition run (17 × 6 sensing devices; total: 102 spin valves) to facilitate the fabrication and ensure device uniformity. All spin valves in the array have the same EB direction and reveal a GMR effect with a magnitude of about 4% (Fig. 3A).

Following sample characterization, the sensors on a foil are delaminated from the rigid support and individually placed in a way that their EB axis is aligned accordingly to the position within the Wheatstone bridge (Fig. 3B). Afterward, the spin valves are contacted to the underlying contacts. Finally, a 5-μm-thick encapsulation layer of polydimethylsiloxane (PDMS) is spin-coated on top and serves as basic encapsulation and soft interface to skin. A scanning electron microscopy (SEM) investigation of the sample cross section [prepared using a focused ion beam (FIB) etching through the layer stack] reveals that the metal layer is firmly attached to the polymer and follows the surface morphology (Fig. 2A, VIII). No cracks in the spin valve or delaminated regions were observed when investigated at different locations of the sample. We note that bonding of the sensor chips on 1.7-μm-thick foil to the extended 1.7-μm-thick supporting foil results in a perfectly homogeneous polymeric layer with a total thickness of about 3.5 μm at the sensor location. No boundary between the two foils is visible in the SEM image, which is crucial to assure mechanical integrity of the entirely flexible device. The device is submerged in water for about 10 min to obtain freestanding 2D sensors (Fig. 2B).

Table 1. Comparison of commercial polymers with the novel ultrathin polyimide foils. The table summarizes the most important parameters involved in our study, such as thickness (*t*), glass transition temperature (T_g), melting temperature (T_m), breaking temperature (T_{br}), and cross-sectional area (*A*).

Polymer	*t* (μm)	T_g (°C)	T_m (°C)	T_{br} (°C)	*A* (m^2)
PET	100	73.3 (*38*)	250 (*38*)	75	2×10^{-6}
PEEK	100	145 (*39*)	340 (*39*)	150	2×10^{-6}
Mylar	2.5	73.3 (*38*)	250 (*38*)	140	5×10^{-8}
This work	1.7	300	325	344	4×10^{-8}

The mechanical stability of the 2D sensors upon bending is tested by placing them onto adapters with predefined curvature radii. Bending down to a curvature of 1 mm does not change the response of the sensing layer and the overall GMR performance of the sensor (Fig. 3A and fig. S2). Their operating range as angle sensors corresponds to the plateau between 20 and 120 Oe, where the spin valves present an almost flat response (no variation of the resistance) as a function of the magnetic field. This condition renders our devices ideal for angle sensing, because the only parameter determining the resistance in this magnetic field range is the angle of the incident field. Our sensors intimately conform to a hair (diameter of about 50 μm; Fig. 2C and fig. S3) and a doctor blade (diameter of about 10 μm; Fig. 2D), demonstrating bending into curvatures smaller than 1 mm. The ultrathin sensor design complies with the surface of a doctor blade even at its apex. Even these extreme bending trials do not impair the GMR performance of our sensors, and no signs of degradation of the metal films, for example, cracks or layer stack delamination, are observed. This remarkable mechanical performance enables the sensor to be readily applied as on-skin electronics with magnetic functionality (Fig. 2, E and F). The GMR response of a spin valve sensor on the middle joint of a finger is shown in movie S1. In the absence of an external magnetic field, a repeated movement of the finger does not alter the sensor response. Signal change is observed only when the functional element is exposed to a magnetic field, that is, of a permanent magnet.

The 2D sensor relies on a nested configuration to connect two Wheatstone bridges (*24*, *25*). Each of the bridges includes four spin valve sensors, which are oppositely biased with respect to their adjacent neighbors (Fig. 3B). This placement of the spin valve sensor elements allows us to achieve a bipolar output, where the full signal amplitude is that of a single element. In addition, because of the Wheatstone configuration, the temperature dependence of a single flexible sensor is canceled out and their intrinsic output offset is removed (*26*, *27*). The inner bridge outputs a voltage V_{cos} proportional to the cosine of the angle θ between the bridge magnetization axis and the orientation of the external magnetic field (inset in Fig. 3B). Analogously, the outer bridge produces a voltage V_{sin} proportional to

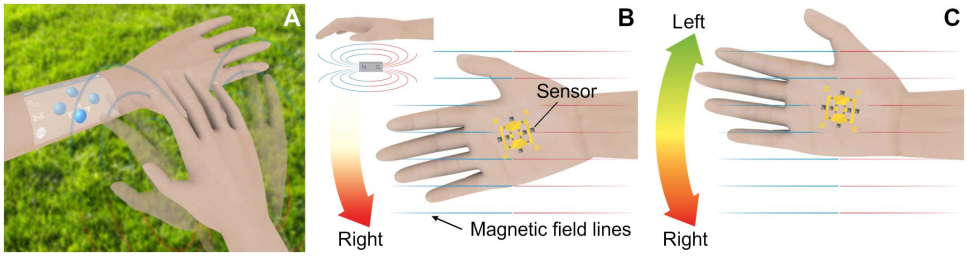

Fig. 1. Touchless manipulation of objects based on the interaction with magnetic fields. (**A**) Concept of touchless manipulation of an object on a (wearable or virtual) screen by moving a hand. (**B** and **C**) An on-skin magnetic field sensor is applied to a palm of the hand. Its angular position with respect to the direction of the external magnetic field is monitored and is used to reconstruct the spatial position of the hand. This information can be used to display the position of the hand in a virtual reality scene or/and to enable interaction with objects in virtual or augmented reality.

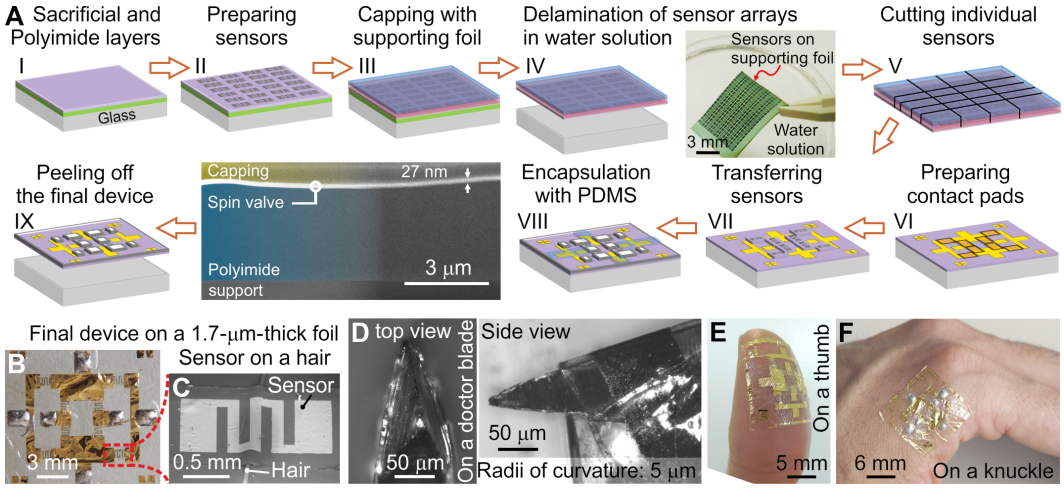

Fig. 2. Fabrication and compliancy characterization of a 2D magnetic field sensor on ultrathin polyimide foils. (**A**) Schematic summary of the key fabrication steps to prepare a 2D magnetic field sensor on ultrathin polyimide foils. An SEM image of the sample cross section reveals the complete layer stack consisting of a novel polyimide foil covered with a firmly attached 27-nm-thick sensing layer, which follows the surface morphology (A, VIII). The total thickness of the polymer is about 3.5 μm, including two bonded 1.7-μm-thick foils. The resulting polymeric layer is perfectly homogeneous and the bonding plane cannot be resolved. (**B**) Optical microscopy image of a 2D sensor containing two Wheatstone bridges accommodating in total eight spin valves properly arranged with respect to their EB direction. An individual spin valve element can compliantly cover a hair (diameter, 50 μm) or a doctor blade (diameter, 10 μm) as shown in (**C**) and (**D**), respectively. (**E** and **F**) Photographs of the entire 2D sensor conveniently placed on skin.

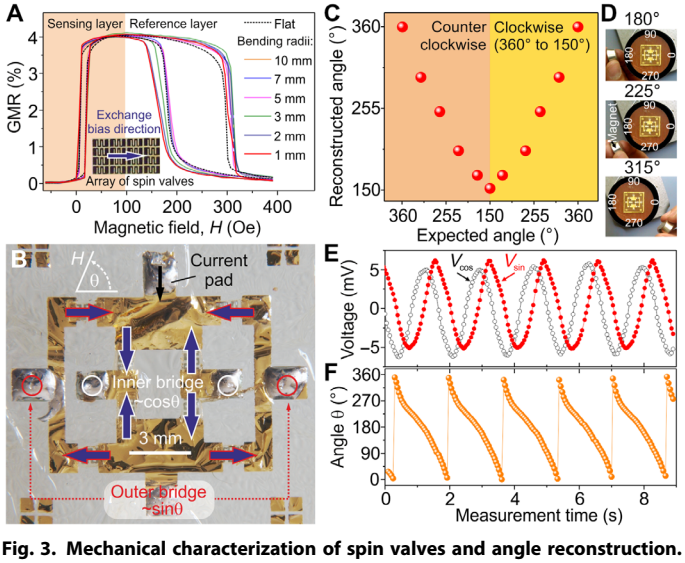

Fig. 3. Mechanical characterization of spin valves and angle reconstruction. (**A**) GMR performance of an individual spin valve sensor. The magnetic field is applied along the EB direction. The sensor response (properties of the sensing layer, orange shaded region) does not change when the sensor is bent down to a radius of curvature of 1 mm. An array of spin valve sensors prepared on thermally stable polyimide-based ultrathin foils is shown as inset in (**A**). The EB direction is set in the same direction for all the sensors in the array. (**B**) Individual spin valve sensors are arranged with respect to their EB direction in two Wheatstone bridges each containing four spin valve sensors to realize a 2D magnetic field sensor. The response of the inner/outer Wheatstone bridge (indicated in white/red) is proportional to the cosine/sine of the angle θ between the bridge magnetization axis and the orientation of the external magnetic field, *H*. (**C**) Reconstruction of the magnetic field angle. The measurement is carried out using a 2D magnetic field sensor transferred to a rigid flat support (after being peeled off). (**D**) Geometry of the experiment: The signal of the Wheatstone bridges depends on the orientation of a permanent magnet. (**E**) Characterization of the 2D sensor. Voltage output signals of the inner (V_{cos}) and outer (V_{sin}) Wheatstone bridges of the 2D sensor. The period of the signals closely corresponds to the rotational speed set by the software (1.6 revolutions/s). There is a phase shift of 90° between the inner and outer bridge signals, which allows the reconstruction of the angle of the magnetic field (**F**).

the sine of θ. With these two output signals, the angle θ is readily determined via $\theta = \arctan(V_{sin}/V_{cos})$. Our sensors thus reconstruct the angle of an external magnetic field, in this case, the one given by a permanent magnet (reconstructed angle plotted against measured angle shown in Fig. 3C).

We perform real-time reconstruction of the magnetic field angle by monitoring the sensor response to a magnetic field of a continuously rotating magnet (fig. S4 and movie S2). By rotating the magnet at a constant rotational speed of 1.6 revolutions/s, a sinusoidal response from each of the bridges is obtained (Fig. 3E) and the angle of the magnetic field can be reconstructed in real time (Fig. 3F). We find a clear 90° phase shift between the outputs of the bridges (Fig. 3E). Each of the acquired signals is fit to a sine function with a standard error of at most 4×10^{-4}.

In addition to exposing the sensor to a homogeneous field of a permanent magnet rotating with a constant speed, we validate the operation of our devices with irregular external magnetic fields that would typically occur in realistic settings of a wearable gadget. Here, we monitor the response of the sensor when exposed to a field of a permanent magnet directly moved by hand. The sensor provides an unambiguous angle reconstruction independent of the tilt angle of the permanent magnet or variations of the distance between the magnetic source and the sensor (movie S3).

The extreme flexibility of our magnetosensitive foils eases the integration with soft and malleable materials such as elastomers and textiles for wearable electronics (*28*–*31*). In this way, the typically somatic interaction with wearable devices (*32*) can be readily extended toward entirely touchless interfacing.

Virtual keypad applications

We devise a demonstrator where the sensor is mounted on an elastic wristband to create a device capable of transducing local magnetic fields into discrete values. A permanent magnet providing magnetic input is attached to the index finger of a volunteer, who then places his finger above distinct angular positions of the sensor. The local in-plane magnetic field changes at these locations and the sensor converts the magnet positions into predefined characters, thereby turning the wristband

into a virtual keypad, which is addressed in a touchless manner. We encode the characters "+," "9," "4," and "1" to the angular segments around 270°, 180°, 90°, and 0°, respectively (Fig. 4A). Approaching the wristband with the finger at given angles allows one to type a predefined sequence of symbols, for example, the initial part of a phone number, +4914… (Fig. 4B and movie S4).

Interactive light dimming by touchless manipulation

The on-skin directional sensors allow one to control a physical property of an object in virtual reality, relying on the interaction with magnetic fields exclusively. We develop a demonstrator based on a magnetic source made of a plastic ring-like support with a permanent magnet in the middle. One of our angle sensors is fixed to the palm of a hand and connected to a computer for visualization purposes. The software encodes the angles received into seven luminescence regions. Each of the regions corresponds to a particular light intensity translating into control of an on-screen virtual light source. The visual representation also includes a virtual dial corresponding to the current position of the hand on the physical magnetic dial. Here, angles between 0° and 180° are encoded to replicate the typical movement of a hand when operating a real dial. This allows us to realize a light-dimming application of a virtual bulb, manipulated solely upon rotation of a volunteer's hand above a magnetic source (Fig. 5 and movie S5).

Because of the PDMS encapsulation, the flexible devices reveal a stable response even when submerged for several minutes in deionized water and a sweat-like saline solution of 40 mM chloride (fig. S5 and movie S6). Long-term stability studies are currently underway. These initial results make us confident that our sensor platform is a viable solution for wearable magnetic field–based interfaces.

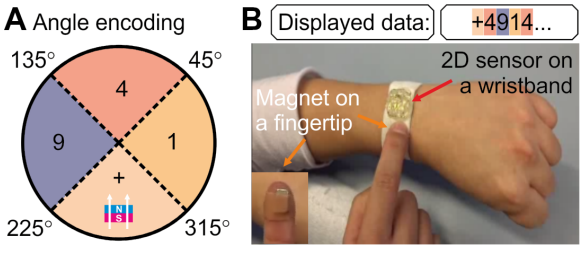

Fig. 4. Virtual keypad addressed in a touchless manner. (**A**) The characters "+," "9," "4," and "1" are encoded in angular segments around 270°, 180°, 90°, and 0°, respectively. (**B**) Photograph showing a 2D sensor mounted on an elastic wristband resembling a virtual keypad. The encoded symbols are displayed when a corresponding angular segment of a sensor is exposed to a magnetic field of a small permanent magnet at the fingertip (movie S3).

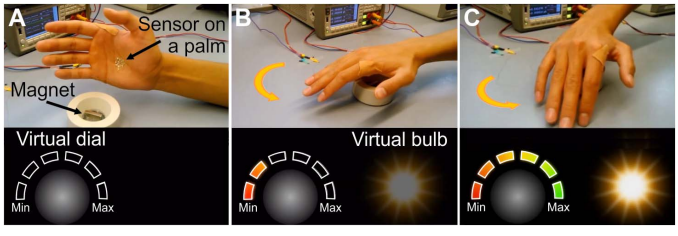

Fig. 5. Light dimming of a virtual bulb. (**A**) Skin-applied 2D sensor as on-skin electronics with directional perception. (**B** and **C**) Movie snapshots demonstrating touchless manipulation of a virtual object using our on-skin 2D magnetic field sensor. The hand is turned with respect to the direction of the magnetic field lines of a permanent magnet. This motion of the hand is monitored and the angular position is transformed into the setting of a virtual dial, in turn controlling the light intensity of a virtual bulb (movie S4).

CONCLUSION

In conclusion, we realized the first mechanically imperceptible e-skins with directional perception. In conjunction with a magnetic field originating from a permanent magnet, the device monitors the motion of a hand based on the interaction of the 2D magnetic field sensor with the magnetic stray field landscape. We demonstrate the potential of our 2D magnetic field sensor platform for augmented reality systems to achieve virtual knob-turning and pressing functions and enable the operation of virtual dialing pads without the use of bulky optical equipment. At present, our devices operate based on the interaction with a magnetic field of a permanent magnet of about 50 Oe. We envision that by improving the flexible sensor technology even further, wearable magnetic sensorics will operate in the geomagnetic field. Our technology platform is based on transfer printing of individual sensor elements and is thus readily extendable to form sensor arrays. Taking advantage of stretchable interconnects, distributed arrays of angle sensors would provide means to perform triangulation tasks or similar motion monitoring duties.

MATERIALS AND METHODS

Fabrication of flexible angle sensors

The magnetic layer stack was deposited onto lithographically defined areas on a 1.7-μm-thick polymeric foil. The foil was laminated onto a sacrificial layer-coated glass slide (Fig. 2A, I and II) for processing. Following sample characterization, dicing tape was applied to the sample covered with a photoresist to aid as support for the transfer process (Fig. 2A, III). The final stack was left in diethylenetriaminepentaacetic acid (DETPA) until the sacrificial layer was dissolved and the remaining part of the stack was released from the glass (Fig. 2A, IV). The free-standing tape containing the sensors was blade-cut into single chips (Fig. 2A, V), which were then transferred to the patterned contacts (Fig. 2A, VI). The transfer of the spin valve chips to the contacts was done by drop-casting liquid polyamic acid on each of the predetermined sites for the sensors (Fig. 2A, VII). Then, the sensors were placed on the droplets and their EB axis was aligned accordingly to the position within the Wheatstone bridge (Fig. 3B). Afterward, the contacts and sensor were soft-baked to evaporate the solvent from the liquid polymer. Then, the bonding polymer droplets were annealed at above 200°C to initiate the imidization process, leading to the hardening of the polymer. Afterward, the device was placed in acetone to remove the photoresist and delaminate the dicing tape, resulting in a fully bonded sensor. After bonding, the spin valves were contacted to the underlying contacts. The output regions of the contact pads were subsequently covered with dicing tape. A 5-μm-thick encapsulation layer of PDMS was spin-coated on top and serves as a soft interface to skin. An SEM investigation of the sample cross section (prepared using a FIB etching through the layer stack) reveals that the metal layer was firmly attached to the polymer and follows the surface morphology (Fig. 2A, VIII). We note that for the FIB/SEM characterization, the samples were capped with a 5-nm-thick Cr layer to avoid charging. There were no cracks in the spin valve or delaminated regions observed when investigated at different locations of the sample. We note that bonding of the sensor chips on 1.7-μm-thick foil to the extended 1.7-μm-thick supporting foil results in a perfectly homogeneous polymeric layer with a total thickness of about

3.5 μm at the sensor location. There was no boundary between the two foils visible in the SEM image, which was crucial to assure mechanical integrity of the entirely flexible device. The device was submerged in water for about 10 min to obtain freestanding 2D sensors (Fig. 2B), followed by peeling off the foils from the rigid glass support (Fig. 2A, IX).

Synthesis and preparation of a polyimide foil

Photosensitive polyimide was synthesized as follows (*33*, *34*): 3,3′,4,4′-biphenyltetracarboxylic dianhydride was reacted with 4,4′-diaminodiphenylmethane in dimethylacetamide (DMAc), modified with dimethylaminoethyl methacrylate and photosensitized using 2 weight % 2-benzyl-2-(dimethylamino)-4-morpholinobutyrophenone (Sigma-Aldrich). The polymer synthesis was performed by dissolution of 9.93 g of 3,3′-diaminodiphenylsulfone in 20 ml of DMAc with the subsequent addition of 12.8 g of 3,3′,4,4′-biphenyltetracarboxylic dianhydride. After mixing for 12 hours at 70°C, the solution of polyamic acid in DMAc was obtained. The solution was modified by reaction with 12.5 g of dimethylaminoethyl methacrylate. The final polyamic acid solution was spin-coated on 22 mm × 22 mm glass slides (VWR International) at 3000 rpm for 40 s with a previous acceleration step of 5 s up to 500 rpm. The polymer-coated glasses were then heated up at 200°C for 10 min under N_2 to imidize and therefore form a stable polyimide film. The final film thickness under these conditions was measured to be 1.7 μm.

Elaboration of electrical contacts

Following the polyimide film preparation, conventional lift-off photolithography (AR-P 3510 photoresist; 3500 rpm, 35 s) was performed to pattern [Ta(5 nm)/Au(100 nm)] contacts on top of the foils. The contact deposition was carried out using magnetron sputtering at room temperature (base pressure: 5×10^{-7} mbar; Ar sputter pressure: 1×10^{-3} mbar; deposition rate: 0.41 Å s^{-1} for Ta and 1.5 Å s^{-1} for Au).

Elaboration of sensor chips

The same 22-mm × 22-mm glasses as used before were left in an aqueous 2% Alconox detergent solution for 2 hours to make the glass surface hydrophilic. Afterward, polyacrylic acid (Polysciences Inc.) was spin-coated on the glasses at 3000 rpm for 30 s, dried at 60°C for 5 min, and subsequently cross-linked by rapid dipping on a 2 M $CaCl_2$ solution. Above this layer, polyamic acid was spin-coated and imidized as described above during the preparation of a foil. On top of the resulting foil, meander sensor structures were patterned at a second lithographic step and a multilayer spin valve stack of [Ta(5 nm)/Py(4 nm)/CoFe(1 nm)/Cu(2.4 nm)/CoFe(1 nm)/Py(4 nm)/IrMn(8 nm)/Ta(2 nm)] was magnetron sputter–deposited at room temperature (base pressure: 3×10^{-7} mbar; Ar sputter pressure: 7.5×10^{-3} mbar; deposition rate: 1 to 2 Å s^{-1} depending on the material) (*35*). Two permanent magnets were mounted on the sample holder to define the EB direction of the sensors. The resulting spin valve arrays were covered with AR-P 3510 photoresist by spin coating (3000 rpm for 35 s followed by 5 min drying at 50°C). Next, standard blue dicing tape was laminated on the stack to aid as a support to ensure further steps of the transfer process. The final stack was left in DETPA for at least 24 hours, until the polyacrylic acid was fully dissolved and the remaining part of the stack was released from the glass. The freestanding tape containing the sensors was blade-cut into single spin valve sensor chips, which were then transferred to the previously patterned contacts. Individual GMR sensor elements were characterized at room temperature by locating the sensor between the pole shoes of an electromagnet. The magnetic field was applied in the sensor plane along the EB direction, and the change of the electrical resistance was measured as a function of the applied magnetic field. The GMR ratio was defined as the magnetic field–dependent change of the sample's resistance, $R(H_{ext})$, normalized to the resistance value of the magnetically saturated sample, R_{sat}: $\mathrm{GMR}(H_{ext}) = [R(H_{ext}) - R_{sat}]/R_{sat}$.

Sensor transfer to the contacts

The transfer of the spin valve chips to the contacts was done by drop-casting liquid polyamic acid on each of the predetermined spots for the sensors. Then, the sensors were carefully placed on the droplets and aligned to fit their corresponding magnetization and position within the Wheatstone bridge design. Afterward, the contacts + sensor were placed in between two flat glasses and pressed with a 500-g weight for 5 min at 50°C to evaporate the solvent from the liquid polymer. Following this preheating, the samples were further pressed in the same way but at 140°C for 10 min to imidize the bonding polymer droplets. The resulting sensor was left to cool down and then placed in acetone for 2 min to remove the photoresist and delaminate the dicing tape, leaving a fully bonded sensor.

Sensor contacting and encapsulation

After bonding, the spin valves were contacted with G3303B silver paste (Plano GmbH) to the underlying contacts. The output regions of the contacts were subsequently covered with dicing tape, and a 5-μm-thick encapsulation layer of PDMS was spin-coated on top (6000 rpm, 5 min). Finally, the finished sensor was left to dry for 24 hours at room temperature to cure the PDMS and complete the elaboration process.

Mechanical performance of the sensors

To analyze the stability of the devices upon bending and the adhesion properties of the metal films to the polymeric support, we carried out several cuts using FIB at different locations over the sample. No signs of delamination of the metal layer from the polymer were found. Furthermore, we studied the mechanical integrity of our devices upon bending into radii below 100 μm. To achieve these small bending radii, we laminated our flexible devices onto a prestretched very high bond (VHB) elastomer, inducing wrinkling of the sensor upon strain relaxation of the elastomer (*4*). In this way, we achieved sub–10-μm bending radii. The wrinkled structures were studied using SEM following FIB cutting of the samples. Even when bending down to radii of about 30 μm, the film remained intact (fig. S6). If the radius of curvature reaches below 10 μm, we could occasionally identify cracks in the film (fig. S7).

By using an ultrathin (1.7 μm thick) substrate, the strain in the metallic spin valve film was greatly reduced. This directly follows from analytical mechanical considerations for foldable film-on-foil electronics (*36*). Here, the strain ε_{top} in a rigid film (Young's modulus, E_f; thickness, t_f) on a softer substrate (Young's modulus, E_s; thickness, t_s) was computed when bending down to a radius R via

$$\varepsilon_{top} = \frac{(t_f + t_s)}{2R} \frac{(1 + 2\eta + \chi\eta^2)}{(1 + \eta)(1 + \chi\eta)}$$

with $\eta = t_f/t_s$ and $\chi = E_f/E_s$. For the polyimide foil in this work, the corresponding parameters were $E_s = 3$ GPa and $t_s = 3400$ nm (two bonded

polyimide layers with each layer being 1700 nm thick). Furthermore, we derived the elastic moduli of the spin valve layer (total thickness: t_f = 27.4 nm) by its material composition to be 167 GPa (7-nm-thick Ta: E_{Ta} = 186 GPa, 8-nm-thick Py: E_{Py} = 120 GPa, 2-nm-thick CoFe: E_{Co} = 209 GPa, 2.4-nm-thick Cu: E_{Cu} = 130 GPa; 8-nm-thick IrMn: E_{Mn} = 209 GPa).

Using the model (*36*) and considering that the film withstands bending to radii of at least 30 μm, we estimated the strain in the layer to be at maximum 4%. This rough estimate was already near the fracture strain even for Cu. Other relaxation mechanisms, for example, reducing the film area due to patterning and edge roughness, were considered to further reduce the strain in the metal film.

We note that increasing the thickness of the polyimide substrate to that of a thin commercial foil (25 μm) will increase the resulting strain up to 40%, values that would result in cracking of the metallic film. These estimations further corroborate the importance of reducing the substrate thickness to improve the overall mechanical performance of the sensors.

Practical applications in wearables will benefit from laminating our ultrathin sensor foils to thin sheets of soft elastomers as strain-buffering interfaces to human skin. As detailed below, an approximately 100-μm-thick PDMS sheet would be sufficient to place the spin valve sensors into the neutral mechanical plane *b*, greatly reducing the bending-induced strain on the metallic layers (*37*)

$$b = \frac{\sum_{i=1}^{n} \bar{E}_i t_i \left(\sum_{j=1}^{i} t_j - \frac{t_i}{2} \right)}{\sum_{i=1}^{n} \bar{E}_i t_i}$$

$$\bar{E}_i = \frac{E_i}{1 - \nu_i^2}$$

where E_i, t_i, and ν_i are the Young's modulus, thickness, and Poisson's ratio of the layer *i* in the stack of layers forming the sensor, respectively. *b* is the height from the bottom of the stack at which the mechanical neutral plane was found in a multilayer system. The PI film and the spin valve were considered as a single layer with a weighed equivalent Young's modulus E_1 = 4.31 GPa and Poisson's ratio ν_1 = 0.34. PDMS as the soft layer has E_2 = 1.84 MPa and ν_2 = 0.5. With these parameters, the mechanical neutral plane *b* was located at about 1.7 μm from the bottom of the stack, right where the spin valve lies. For nonideal situations where the spin valve is at a distance δ from the neutral plane, we would arrive at a strain of $\varepsilon = \frac{\delta}{r}$, with *r* being the curvature radius. We note that placing the sensor foil on prestretched VHB tape to form a wrinkled structure (and thus a stretchable sensor) will likewise move the active spin valve close to the neutral plane, because the VHB elastomer used in these experiments has a similar Young's modulus and a thickness in the range of 50 to 100 μm.

Another strategy to improve the strain tolerance of our sensors is to use a 1.7-μm-thick polyimide layer as encapsulation, as the now matching Young's moduli of the substrate and encapsulation will place the spin valve again in the neutral mechanical plane and thus allow extreme flexibility without damage to the sensor layer.

Sinusoidal angle characterization

To measure the dependence of the sensor output signals on the in-plane magnetic field angle, we devised a motorized setup that consists of a rotating permanent magnet placed underneath a plastic disk-like sample holder. The magnet was fixed to the shaft of a stepper motor (Trinamic PD3-110-42) in such a way that the uniform field lines lay parallel to the plane of the sample, therefore allowing a controlled rotation of the in-plane field. Furthermore, the sample holder was fixed 9 cm over the magnet with an extension clamp to ensure a constant field of 50 Oe, as measured with an HG09 gaussmeter (Goudsmit Magnetic Systems). We note that this field falls inside the ideal operation region of our spin valves (20 to 120 Oe).

When conducting this experiment, we made sure that the characterization setup used to measure the sensor was designed such that the in-plane field had a variation of less than 300 μT within the area of the sensor (fig. S8). This arrangement was achieved by first determining the best geometry and placement for the magnet to generate a constant field over a large enough area to cover the entirety of the sensor. Then, we verified that the magnetic field within the sensor plane varies only minimally (less than 300 μT) using a gaussmeter.

The sensor was then placed on the holder and connected to two B2902A Source/Measure Units (Keysight Technologies). One of the units was used to source a constant voltage of 1 V to bias the sensor and the other one was used to measure the outputs of each of the two nested bridges. The unit in charge of the measurements was remotely programmed and controlled with custom software, which acquires the output voltages of the sensor, computes the corresponding angle value, and visualizes the resulting real-time signals on screen. By using the stepper motor's software (TMCL-IDE version 3.0.10.0) to drive the motor at a constant rotational speed, we measured a sinusoidal response from each of the bridges with the expected 90° phase shift between outputs. The rotational speed of the stepper motor was set to 1.6 revolutions/s to facilitate the display and analysis of data. Each of the acquired signals was fit to a sine function to determine how much they resembled the ideal case. We found that for a standard fitting function of the form $y = y_0 + A \sin[\pi (x - x_c)/w]$ (*A*, amplitude of the peak and *w*, peak width), the standard error was 0 for all parameters but *w*, for which the error was only 4×10^{-4}. These results were obtained in both the pretransfer and posttransfer states.

Angular resolution of the device

The angular resolution can be estimated using the intrinsic noise of the sensor and the total voltage range over 180°. We observe a measurement noise of 200 μV_{pp} (after software filtering), which, together with a detection range of 180°/5 mV_{pp}, yields an effective resolution of about 7°.

This would, in principle, allow one to encode more angles, but there are additional factors to be taken into account. These are (i) the output voltage offset, (ii) the transition regions between encoded values, and (iii) the size and shape of the source magnet used to actuate the sensor.

The output voltage offset is crucial as the angle is reconstructed from $\theta_{rec} = \arctan(V_{sin}/V_{cos})$. Under ideal circumstances, V_{sin} and V_{cos} have the form $A \sin\theta$ and $A \cos\theta$, with *A* being the signal amplitude. However, upon the introduction of an offset, they become $A \sin\theta + V_{sin\_off}$ and $A \cos\theta + V_{cos\_off}$, resulting in a less trivial reconstruction $\theta_{rec} = \arctan(A \sin\theta + V_{sin\_off}/A \cos\theta + V_{cos\_off})$. Therefore, it is crucial to include offset compensation. We use a software-based compensation scheme that updates itself at every run to cancel out the V_{sin} and V_{cos} offsets.

The transition regions are required to leave enough spacing between the encoded values and avoid cross-talking between two adjacent values. Angles falling inside these regions are not encoded and thus serve as separators. If we determine the transition regions to be two times the angular resolution (=14°), we can calculate a theoretical maximum for the number of encoded values by assuming the case when the span

of the transition region equals that of the encoding region. In this case, the total number of sectors is given by 360°/14° = 25, and because half of them are used as transition regions, we arrive at a maximum of 12 values that can be reliably encoded.

The size of the magnetic flux area and the uniformity of the magnetic source (permanent magnet attached to the finger in Fig. 4B) are additional aspects to be considered. If the area of influence of the source is larger than the physical area spanned by a particular encoded value, cross-talk will occur even if the sensor performs as desired. Also, if the magnet is too small (comparable to a single spin valve), it will not be able to activate all spin valves simultaneously and the reading will be inaccurate. We therefore used a magnet size that allows an efficient reading for a 90° spacing. However, reducing the size of the magnetic flux area is possible (here, by about four times), allowing encoding of up to eight values. Further expansion of the values is feasible and will require additional optimization of the encoding and the magnetic source.

Manual angular characterization

In addition to characterizing the full-scale response of the imperceptible angle sensor, we studied the sensor response to discrete angular steps with the aim of verifying the correspondence of the measured angles with the software-calculated ones. For this experiment, the sensor was fixed to the center of the sample holder and a permanent magnet was placed at different angles along the perimeter of the holder. The magnet was rotated around the sample while keeping a distance of about 2.5 cm to the sample's center to provide a field of 50 Oe at each angle. The selected angles were spaced 45° from each other starting at 0° and going in a clockwise direction up to 180°; the last step was measured at 150°. All of the procedure was simultaneously captured on video. Then, the video was analyzed to extract the angular placement of the magnet. This angle was plotted against the measured angle to determine their resemblance. The data from these measurements revealed good correspondence between the reconstructed and the measured angles.

Temperature stability of the polymeric support

We developed ultrathin polyimide foils that are about 1.7 µm thick and have a very small surface roughness of about 1 nm (fig. S9). This is absolutely necessary for the successful growth of the high-performance magnetic sensor layer. The foils offer good adhesion for functional elements processed on it using standard deposition and lithography techniques (see, for example, Fig. 2B). The synthesized polymeric foil reveals remarkable thermal stability, even allowing for regular soldering to be performed. In the following, we characterize the thermal stability of the polymeric support and compare it to the commercially available counterparts. For this study, we devised a strain-temperature experiment at constant stress. To have well-characterized references, we used standard high-performance polymer films such as 100-µm-thick polyethylene terephthalate (PET), 100-µm-thick polyetheretherketone (PEEK), and 2.5-µm-thick Dupont Mylar. In this experiment, the films were vertically fixed with a spring clip to a clamp stand and pulled downward by another 10 g of spring clip, which provided constant stress during the measurements (inset in fig. S10A). Then, the films were heated up progressively with a ZD-939L hot air rework station (Ningbo Zhongdi Industry & Trade Co.) until they reached their breaking point. The heat was supplied through a 4-mm-diameter nozzle for ultrathin foils (2.5-µm-thick Mylar and the polymeric foil synthesized in this work) and without a nozzle (2.1-mm heating diameter) for 100-µm-thick samples. The reason for this heating area modification was to assure that the thinnest samples remained perpendicular to the temperature source without being pushed away by an excessive airflow. Next, the behavior of the films was captured on video to determine their deformation upon heating. The quantitative deformation analysis was done by comparing the length L of the films at each of the frames of the video with their original length L_0. Using this information, we calculated the elongation as $(L - L_0)/L_0$ as a function of temperature for each of the investigated polymer films. By plotting the elongation as a function of the temperature, we observed that our polyimide foils can withstand temperatures up to 344°C, at which point it finally breaks. This performance is quite remarkable given that its cross-sectional area is two orders of magnitude smaller than that of the other evaluated polymers except for Mylar. Thicker polymers such as PET and PEEK could not reach more than 150°C without breaking, and Mylar, the ultrathin version of PET, could not withstand temperatures beyond this. Considering the small thickness of the foil, loading it with 10 g corresponds to a surface pressure of 58 kPa·m. In addition to this rather high pressure, the foil withstands temperatures of up to 340°C (fig. S10A) by far outperforming commercially available PET foils (movie S7). This remarkable thermal stability of a 1.7-µm-thick foil allows for a regular soldering of electrical contacts directly to the lithographically defined contact pads (fig. S10, B and C). An SEM image of the sample cross section reveals that the contact pad is firmly attached to the polymer even when in the direct vicinity of the soldered contact (fig. S10, D and E).

Another observation from this experiment is that our polyimide foil presents an S-shaped deformation curve (fig. S11) with a sudden increase before 100°C, a stable plateau between 100° and 300°C, and finally a steep increase up to 344°C, when it breaks. This behavior suggests that during the first transition, the polymer dries and excess solvent is removed. Then, chain elongation ensues and stabilizes during the observed plateau when the polymer reaches its final hard and stable form. Finally, as the temperature further increases, the film becomes more fluid as it approaches its melting point and a sudden deformation follows. At this point, the constant stress causes substantial necking on the polymer film, which further debilitates its structure and triggers its final rupture before reaching the melting point. In necking, the cross-sectional area of a material is reduced faster than its hardening ratio, causing a concentration of the strain in the regions of highest stress. For our experiments, this change in the cross-sectional area was mediated by the decreasing polymer's viscosity as the temperature was increased. This deformation mode can explain the premature failure of the other polymer films studied, which also experienced a decrease in local cross-sectional area before their melting point.

Temperature compensation of the sensor bridge

We characterized the response of a single spin valve sensor and a sensor bridge upon heating using a heat gun. A single sensor strongly responds even to slight temperature variation; however, no change in the readout of the bridge is observed upon the same heat treatment (fig. S12 and movie S8).

This behavior arises from the intrinsic compensation properties of the Wheatstone bridge. The typical output characteristic V_{out}/V_{bias} of a Wheatstone bridge with resistors R_1 to R_4 can be written as follows

$$\frac{V_{out}}{V_{bias}} = \frac{R_1}{R_1 + R_2} - \frac{R_4}{R_3 + R_4} = \frac{R_1{*}R_3 - R_2{*}R_4}{(R_1 + R_2)(R_3 + R_4)}$$

If $R_1 = R_3 = R_2 = R_4 = R_0$, the output voltage is 0 and the offset is fully compensated. In reality, however, the resistors vary (for example, with temperature) and produce unwanted offsets. Assuming the case of varying resistors, with $R_1 = R_3 = R_2 = R_4 = R_0$ and a variation smaller than the nominal value of the resistors, second-order terms can be neglected and the output can be written as

$$\frac{\Delta V_{out}}{V_{bias}} = \frac{\Delta R_1 - \Delta R_2 + \Delta R_3 - \Delta R_4}{4R_0}$$

If the resistance variation is produced by the change of temperature ΔT, it can be written as $\Delta R = R_0 \alpha \Delta T$ (α is the temperature coefficient of resistivity)

$$\frac{\Delta V_{out}}{V_{bias}} = \frac{R_0 \alpha \Delta T - R_0 \alpha \Delta T + R_0 \alpha \Delta T - R_0 \alpha \Delta T}{4R_0} = 0$$

Because all the elements are expected to respond in the same way to temperature, they compensate mutually and the temperature-induced variations in the output voltage are eliminated.

SUPPLEMENTARY MATERIALS

Supplementary material for this article is available at http://advances.sciencemag.org/cgi/content/full/4/1/eaao2623/DC1

fig. S1. Fabrication flow.
fig. S2. Mechanical characterization of spin valves.
fig. S3. Compliancy of a flexible spin valve to a hair.
fig. S4. Angle characterization setup.
fig. S5. Encapsulation experiments for a spin valve sensor.
fig. S6. Mechanical stability of the sensor layer stack upon bending.
fig. S7. Development of cracks in strongly curved devices.
fig. S8. Schematics of the setup used to measure the angle response of the sensor in a rotating magnetic field of a permanent magnet.
fig. S9. Surface quality characterization.
fig. S10. Thermal stability of the foils.
fig. S11. Elongation of polymeric foil versus temperature.
fig. S12. Temperature compensation of the sensor bridge.
movie S1. Response of a spin valve upon bending.
movie S2. Reconstruction of the magnetic field angle using 2D sensor.
movie S3. Reconstruction of the magnetic field angle under irregular field excitation.
movie S4. Demonstrator 1: Virtual keypad applications.
movie S5. Demonstrator 2: Interactive light dimming by touchless manipulation.
movie S6. Stability of the sensor response submerged in aqueous and saline solution.
movie S7. Temperature stability of the novel ultrathin polyimide foils and a commercial foil.
movie S8. Temperature compensation of the bridge.

REFERENCES AND NOTES

1. J.-W. Jeong, W.-H. Yeo, A. Akhtar, J. J. S. Norton, Y.-J. Kwack, S. Li, S.-Y. Jung, Y. Su, W. Lee, J. Xia, H. Cheng, Y. Huang, W.-S. Choi, T. Bretl, J. A. Rogers, Materials and optimized designs for human-machine interfaces via epidermal electronics. *Adv. Mater.* **25**, 6839–6846 (2013).
2. S. Jung, J. H. Kim, J. Kim, S. Choi, J. Lee, I. Park, T. Hyeon, D.-H. Kim, Reverse-micelle-induced porous pressure-sensitive rubber for wearable human–machine interfaces. *Adv. Mater.* **26**, 4825–4830 (2014).
3. S. Lim, D. Son, J. Kim, Y. B. Lee, J.-K. Song, S. Choi, D. J. Lee, J. H. Kim, M. Lee, T. Hyeon, D.-H. Kim, Transparent and stretchable interactive human machine interface based on patterned graphene heterostructures. *Adv. Funct. Mater.* **25**, 375–383 (2015).
4. M. Kaltenbrunner, T. Sekitani, J. Reeder, T. Yokota, K. Kuribara, T. Tokuhara, M. Drack, R. Schwödiauer, I. Graz, S. Bauer-Gogonea, S. Bauer, T. Someya, An ultra-lightweight design for imperceptible plastic electronics. *Nature* **499**, 458–463 (2013).
5. G. A. Salvatore, N. Münzenrieder, T. Kinkeldei, L. Petti, C. Zysset, I. Strebel, L. Büthe, G. Tröster, Wafer-scale design of lightweight and transparent electronics that wraps around hairs. *Nat. Commun.* **5**, 2982 (2014).
6. M. Drack, I. Graz, T. Sekitani, T. Someya, M. Kaltenbrunner, S. Bauer, An imperceptible plastic electronic wrap. *Adv. Mater.* **27**, 34–40 (2015).
7. M. Melzer, M. Kaltenbrunner, D. Makarov, D. D. Karnaushenko, D. Karnaushenko, T. Sekitani, T. Someya, O. G. Schmidt, Imperceptible magnetoelectronics. *Nat. Commun.* **6**, 6080 (2015).
8. K. Cherenack, C. Zysset, T. Kinkeldei, N. Münzenrieder, G. Tröster, Woven electronic fibers with sensing and display functions for smart textiles. *Adv. Mater.* **22**, 5178–5182 (2010).
9. W. Zeng, L. Shu, Q. Li, S. Chen, F. Wang, X.-M. Tao, Fiber-based wearable electronics: A review of materials, fabrication, devices, and applications. *Adv. Mater.* **26**, 5310–5336 (2014).
10. W. Gao, S. Emaminejad, H. Y. Y. Nyein, S. Challa, K. Chen, A. Peck, H. M. Fahad, H. Ota, H. Shiraki, D. Kiriya, D.-H. Lien, G. A. Brooks, R. W. Davis, A. Javey, Fully integrated wearable sensor arrays for multiplexed in situ perspiration analysis. *Nature* **529**, 509–514 (2016).
11. A. J. Bandodkar, I. Jeerapan, J. Wang, Wearable chemical sensors: Present challenges and future prospects. *ACS Sens.* **1**, 464–482 (2016).
12. S. Choi, H. Lee, R. Ghaffari, T. Hyeon, D.-H. Kim, Recent advances in flexible and stretchable bio-electronic devices integrated with nanomaterials. *Adv. Mater.* **28**, 4203–4218 (2016).
13. J. Kim, D. Son, M. Lee, C. Song, J.-K. Song, J. H. Koo, D. J. Lee, H. J. Shim, J. H. Kim, M. Lee, T. Hyeon, D.-H. Kim, A wearable multiplexed silicon nonvolatile memory array using nanocrystal charge confinement. *Sci. Adv.* **2**, e1501101 (2016).
14. D. J. Lipomi, Z. Bao, Stretchable and ultraflexible organic electronics. *MRS Bull.* **42**, 93–97 (2017).
15. X. Huang, Y. Liu, G. W. Kong, J. H. Seo, Y. Ma, K.-I. Jang, J. A. Fan, S. Mao, Q. Chen, D. Li, H. Liu, C. Wang, D. Patnaik, L. Tian, G. A. Salvatore, X. Feng, Z. Ma, Y. Huang, J. A. Rogers, Epidermal radio frequency electronics for wireless power transfer. *Microsyst. Nanoeng.* **2**, 16052 (2016).
16. T. Yokota, P. Zalar, M. Kaltenbrunner, H. Jinno, N. Matsuhisa, H. Kitanosako, Y. Tachibana, W. Yukita, M. Koizumi, T. Someya, Ultraflexible organic photonic skin. *Sci. Adv.* **2**, e1501856 (2016).
17. A. Chortos, J. Liu, Z. Bao, Pursuing prosthetic electronic skin. *Nat. Mater.* **15**, 937–950 (2016).
18. H. Araki, J. Kim, S. Zhang, A. Banks, K. E. Crawford, X. Sheng, P. Gutruf, Y. Shi, R. M. Pielak, J. A. Rogers, Materials and device designs for an epidermal UV colorimetric dosimeter with near field communication capabilities. *Adv. Funct. Mater.* **27**, 1604465 (2017).
19. T. Someya, S. Bauer, M. Kaltenbrunner, Imperceptible organic electronics. *MRS Bull.* **42**, 124–130 (2017).
20. M. Melzer, J. I. Mönch, D. Makarov, Y. Zabila, G. S. Cañón Bermúdez, D. Karnaushenko, S. Baunack, F. Bahr, C. Yan, M. Kaltenbrunner, O. G. Schmidt, Wearable magnetic field sensors for flexible electronics. *Adv. Mater.* **27**, 1274–1280 (2015).
21. D. Makarov M. Melzer, D. Karnaushenko, O. G. Schmidt, Shapeable magnetoelectronics. *Appl. Phys. Rev.* **3**, 011101 (2016).
22. S. S. P. Parkin, Giant magnetoresistance in magnetic nanostructures. *Annu. Rev. Mater. Sci.* **25**, 357–388 (1995).
23. J. Nogués, I. K. Schuller, Exchange bias. *J. Magn. Magn. Mater.* **192**, 203–232 (1999).
24. A. Johnson, "Spin Valve Systems for Angle Sensor Applications," thesis, Technische Universität Darmstadt, Darmstadt, Germany (2004).
25. O. Ueberschär, M. J. Almeida, P. Matthes, M. Müller, R. Ecke, R. Rückriem, J. Schuster, H. Exner, S. E. Schulz, Optimized monolithic 2-D spin-valve sensor for high-sensitivity compass applications. *IEEE Trans. Magn.* **51**, 4002404 (2015).
26. I. Mönch, D. Makarov, R. Koseva, L. Baraban, D. Karnaushenko, C. Kaiser, K.-F. Arndt, O. G. Schmidt, Rolled-up magnetic sensor: Nanomembrane architecture for in-flow detection of magnetic objects. *ACS Nano* **5**, 7436–7442 (2011).
27. N. Münzenrieder, D. Karnaushenko, L. Petti, G. Cantarella, C. Vogt, L. Büthe, D. D. Karnaushenko, O. G. Schmidt, D. Makarov, G. Tröster, Entirely flexible on-site conditioned magnetic sensorics. *Adv. Electron. Mater.* **2**, 1600188 (2016).
28. K. Cherenack, L. van Pieterson, Smart textiles: Challenges and opportunities. *J. Appl. Phys.* **112**, 091301 (2012).
29. T. Zhou, C. Zhang, C. B. Han, F. R. Fan, W. Tang, Z. L. Wang, Woven structured triboelectric nanogenerator for wearable devices. *ACS Appl. Mater. Interfaces* **6**, 14695–14701 (2014).
30. X. Pu, L. Li, H. Song, C. Du, Z. Zhao, C. Jiang, G. Cao, W. Hu, Z. L. Wang, A self-charging power unit by integration of a textile triboelectric nanogenerator and a flexible lithium-ion battery for wearable electronics. *Adv. Mater.* **27**, 2472–2478 (2015).
31. X. He, Y. Zi, H. Guo, H. Zheng, Y. Xi, C. Wu, J. Wang, W. Zhang, C. Lu, Z. L. Wang, A highly stretchable fiber-based triboelectric nanogenerator for self-powered wearable electronics. *Adv. Funct. Mater.* **27**, 1604378 (2017).
32. M. Billinghurst, T. Starner, Wearable devices: New ways to manage information. *C. R. Geosci.* **32**, 57–64 (1999).

33. D. D. Karnaushenko, D. Karnaushenko, D. Makarov, O. G. Schmidt, Compact helical antenna for smart implant applications. *NPG Asia Mater.* **7**, e188 (2015).
34. D. Karnaushenko, N. Münzenrieder, D. D. Karnaushenko, B. Koch, A. K. Meyer, S. Baunack, L. Petti, G. Tröster, D. Makarov, O. G. Schmidt, Biomimetic microelectronics for regenerative neuronal cuff implants. *Adv. Mater.* **27**, 6797–6805 (2015).
35. M. Melzer, G. Lin, D. Makarov, O. G. Schmidt, Stretchable spin valves on elastomer membranes by predetermined periodic fracture and random wrinkling. *Adv. Mater.* **24**, 6468–6472 (2012).
36. Z. Suo, E. Y. Ma, H. Gleskova, S. Wagner, Mechanics of rollable and foldable film-on-foil electronics. *Appl. Phys. Lett.* **74**, 1177–1179 (1999).
37. C. K. Jeong, K.-I. Park, J. H. Son, G.-T. Hwang, S. H. Lee, D. Y. Park, H. E. Lee, H. K. Lee, M. Byun, K. J. Lee, Self-powered fully-flexible light-emitting system enabled by flexible energy harvester. *Energy Environ. Sci.* **7**, 4035–4043 (2014).
38. Y. Zhang, J. Zhang,Y. Lu, Y. Duan, S. Yan, D. Shen, Glass transition temperature determination of Poly(ethylene terephthalate) thin films using reflection–absorption FTIR. *Macromolecules* **37**, 2532–2537 (2004).
39. P. Cebe, S. Y. Chung, S.-D. Hong, Effect of thermal history on mechanical properties of polyetheretherketone below the glass transition temperature. *J. Appl. Polym. Sci.* **33**, 487–503 (1987).

Acknowledgments: We acknowledge insightful discussions with M. Melzer (IFW Dresden) and S. Bauer (Johannes Kepler University Linz). We thank C. Krien, I. Fiering (both from IFW Dresden), and B. Scheumann [Helmholtz-Zentrum Dresden-Rossendorf (HZDR)] for the deposition of metal layer stacks. Support by the clean room team headed by S. Harazim (IFW Dresden) and by the Nanofabrication Facilities Rossendorf and Structural Characterization Facilities Rossendorf at the Ion Beam Center at the HZDR is greatly appreciated. **Funding:** This work was financed in part via the European Research Council (ERC) within the European Union's Seventh Framework Programme (FP7/2007-2013)/ERC grant agreement no. 306277. M.K. acknowledges funding through the LIT start-up grant LIT013144001SEL. **Author contributions:** G.S.C.B. designed and fabricated the sensors and conducted the experiments. G.S.C.B., M.K., and D.M. analyzed the data and prepared figures with contributions from all authors. D.D.K. and D.K. developed the polyimide foils. L.B. carried out structural characterization of the samples. A.L. measured the mechanical performance of the spin valves. G.S.C.B., M.K., and D.M. wrote the manuscript with comments from all authors. All co-authors edited the manuscript. D.M., O.G.S., and J.F. conceived the project. **Competing interests:** The authors declare that they have no competing interests. **Data and materials availability:** All data needed to evaluate the conclusions in the paper are present in the paper and/or the Supplementary Materials. Additional data related to this paper may be requested from the authors.

Submitted 29 July 2017
Accepted 12 December 2017
Published 19 January 2018
10.1126/sciadv.aao2623

Citation: G. S. Cañón Bermúdez, D. D. Karnaushenko, D. Karnaushenko, A. Lebanov, L. Bischoff, M. Kaltenbrunner, J. Fassbender, O. G. Schmidt, D. Makarov, Magnetosensitive e-skins with directional perception for augmented reality. *Sci. Adv.* **4**, eaao2623 (2018).